Visualizing Ensembles of Viscous Fingers

Guillaume Favelier, Charles Gueunet, Julien Tierny

Visualizing Ensembles of Viscous Fingers

Guillaume Favelier*
Sorbonne Universites,
UPMC Univ Paris 06, CNRS,
LIP6 UMR 7606, France.

Charles Gueunet†
Kitware SAS,
Sorbonne Universites,
UPMC Univ Paris 06, CNRS,
LIP6 UMR 7606, France.

Julien Tierny‡
Sorbonne Universites,
UPMC Univ Paris 06, CNRS,
LIP6 UMR 7606, France.

ABSTRACT

This paper presents a topological data analysis framework based on persistent homology and Morse complexes for the visualization and analysis of ensemble data-sets representing viscous fingers. Our approach quantitatively corroborates the classical description of viscous fingers. A systematic analysis across several data resolutions indicates converging statistics as the resolution increases.

Keywords: Topological data analysis, data segmentation, feature tracking, ensemble data, viscous fingers.

1 INTRODUCTION

Viscous fingering is an instability phenomenon which occurs in porous media at the interface between two fluids of distinct viscosity. In particular, it appears when a less viscous fluid is injected within a more viscous one. It intervenes in many fields of science and engineering [5, 8], including geology, hydrology as well as in oil industry where it plays a key role in the extraction process.

This phenomenon is characterized by the formation of a characteristic pattern, called *viscous fingers* (Fig. 1). In particular, the geometrical evolution of these patterns provides good indications about the evolution of the penetration of the less viscous fluid. Thus, capturing, tracking and analyzing the geometry of viscous fingers is of first importance for the understanding of the penetration process.

Viscous fingering can be decomposed into three major regimes:

1. *Launch:* Initially, the interface between the two fluids is approximately planar. Then, the less viscous fluid starts to penetrate the more viscous one when sufficient injection force is applied to it. Viscous fingers of low and uniform amplitude start to appear in this phase.
2. *Expansion:* Once the reaction is launched, the difference of pressure between the two fluids tends to favor an acceleration of the penetration speed for the areas where the less viscous fluid penetrates the most the more viscous fluid. In other words, larger fingers will tend accelerate and grow faster than smaller ones, resulting eventually in a configuration where only large and elongated fingers prevail (Fig. 1).
3. *Termination:* Optionally, depending on the characteristics of the media and the fluids, the two fluids can eventually mix together in a termination state, where the finger pattern has completely disappeared, after the merge of the large fingers.

Depending on the type of data (acquired or simulated), the robust identification and tracking through time of the fingers for each of these steps is subject to several challenges:

1. The represented fluids or the input data representation may not be conducive to an easy discrimination of the less viscous fluid from the other one.
2. Once the fluids have been separated, the shape of their interface can admit a complex geometry, with several protrusions of a variety of scales, which challenges the clear identification of the individual fingers.
3. Once the geometry of the interface has been extracted, the rapid and non-uniform growth of the fingers challenges their robust tracking through time.
4. Finally, once a reliable tracking of the fingers has been achieved, relevant quantitative statistics still need to be derived and evaluated for the interpretation of the phenomenon.

In this paper, we focus on the viscous fingering simulation data provided in the context of the scientific visualization contest 2016 [9], which on top of the aforementioned challenges, brings an additional level of complexity to the problem by studying ensemble data. This simulation studies viscous fingering in the context of the mix of continuously dissolving salt and water. As further described in [9], the simulation runs are given as time-varying particle data-sets representing salt concentration. Due to the stochastic nature of the simulation algorithm, several runs are considered, at distinct resolutions. This yields the following additional challenges:

1. The overall volume of generated data prevents a fast and easy analysis, visualization and interpretation of the phenomenon.
2. The stochastic nature of the simulation code raises the question of the stability of the fingering process across several runs, which needs to be analyzed.
3. The multi-resolution nature of the data raises the question of the convergence of the simulation code, which also needs to be analyzed.

In this paper, we address the two sets of challenges described above and we present an interactive framework for the analysis and visualization of ensembles of viscous fingers. In particular, we show how to extend and adapt to viscous fingering the data analysis pipeline proposed by Laney et al. [12] in the context of the study of the Rayleigh Taylor instability. Finally we report the findings we made by using our data analysis framework.

2 DATA PRE-PROCESSING

The input data is given by three sets of simulation runs (one set per resolution). Each run is represented by time-varying particles carrying salt concentration. We pre-process each time-step by computing a volumetric interpolation of the particle data onto a 128^3 regular grid. In particular, we use an adaptation of Shepard's kernel method [14] to three-dimensional domains. Next, this regular grid is clipped to the original shape of the domain (a cylinder) to avoid the effects of the boundary on the interpolation (Fig. 2). This results in a tetrahedral mesh that will be the input to our data analysis pipeline (Sec. 3). The advantage of this preprocessing is twofold:

- First, it brings continuity to the data, which enables the usage of a larger class of analysis algorithms.
- Second, it allows for truly interactive renderings of each time step based on volume rendering, isosurfaces or color mapped clipped views for instance.

This pre-processing addresses task 1 of the contest instructions [9].

*E-mail: guillaume.favelier@lip6.fr
†E-mail: charles.gueunet@{kitware.com, lip6.fr}
‡E-mail: julien.tierny@lip6.fr

3 Data Analysis Pipeline

Our data analysis pipeline adapts the approach by Laney et al. [12] to viscous fingering. It is composed of 5 steps, illustrated in Fig. 3, which are described in the following subsections.

3.1 Fluid discrimination (per time-step)

First, for each time step, we separate the dissolving salt from the ambient water. Given the piecewise linear (PL) scalar field f_c representing salt concentration and defined on the tetrahedral mesh $\mathscr{M}$ representing our input domain, we identify as dissolving salt the sur-level set $\mathscr{L}^+$ of f_c at the isovalue i_{salt}:

$$\mathscr{L}^+(i_{salt}) = \{p \in \mathscr{M} \mid f_c(p) \geq i_{salt}\} \quad (1)$$

From our experience, we found that an isovalue i_{salt} of 10 gave consistent results along time steps and across runs. Finally, to ignore spurious bubbles, we only consider in the remainder the largest connected component of $\mathscr{L}^+(i_{salt})$, that we note $\mathscr{S}$ (Fig. 3(a)).

3.2 Finger identification (per time-step)

Next, given the geometry of the dissolving salt $\mathscr{S}$, we aim at extracting in a robust manner the tips of the viscous fingers. To achieve this, we consider as finger tips the points which are locally the furthest away from the top of the domain, where salt is continuously added. Intuitively, this corresponds to salt particles which traveled the furthest from their origin. We model such points as local maxima [1] of the geodesic distance [6] $f_d : \mathscr{S} \rightarrow \mathbb{R}^+$ from the top of the domain. As shown in Fig. 3(b) (small light green spheres), this strategy identifies as finger tip even slight bumps in the geometry. Thus, we employ persistent homology [7] to filter the maxima. In particular, our experience shows that preserving maxima whose persistence is higher than 10% of the function span provides consistent results along time-steps and across runs (Fig. 3(b), large dark green spheres). In practice, the persistence of the maxima is evaluated by applying the Elder's rule [7] during the expansion (in decreasing order of f_d) of a union-find data structure [3].

Next, given the list of finger tips $\mathscr{T}$ previously identified, we compute for each vertex of $\mathscr{S}$, the geodesic distance to its closest finger tip, noted $f_t : \mathscr{S} \rightarrow \mathbb{R}^+$ (Fig. 3(c)). We finally identify as *viscous fingers* each cell of the Morse complex [4] of f_t (Fig. 3(d)). In practice, such cells are evaluated with a watershed traversal [16] initiated at each finger tip. Here, like Laney et al. [12], the usage of the Morse complex enables a complete partitioning of $\mathscr{S}$, with a bijection from the set of partitions to the set of finger tips (in contrast to a Reeb graph [13] based segmentation). However, in contrast to Laney et al. [12], the Morse complex is not computed on the interface between the fluids but on the tetrahedral mesh $\mathscr{S}$, which facilitates the evaluation of volumetric indicators. This step partially addresses the task 2 of the contest instructions [9].

3.3 Finger tracking (per run)

Once fingers have been extracted on a per time-step basis, we proceed to their tracking through time with an approach similar to topology based techniques [2, 15]. In particular, for each finger at a time-step t, we connect it to the finger at time-step $t+1$ which maximizes the volume of their intersection (Fig. 3(e)). Once all the time-steps have been processed, we re-iterate through the list of fingers to give a unique identifier to fingers that are connected through time. If multiple fingers of a time step t connect to a single finger at time step $t+1$, we give it the identifier of the *oldest* of the fingers of time step t. This heuristic is motivated by topological persistence [7] (Elder's rule). Finally, we stop the tracking procedure when fingers hit the bottom of the domain. An example of time-tracking is shown in Fig. 4. The output of our time tracking algorithm is a series of tetrahedral meshes $\mathscr{S}_i$, with a finger identifier defined per vertex. Each of these can be visualized interactively with our system and the users can interactively navigate through the time steps. This finishes to address task 2 of the contest instructions [9].

3.4 Quantitative analysis (per run)

Once the fingers have been tracked through time, various time-varying statistics are computed on a per finger basis, such as the evolution of its volume for instance (see Sec. 5 for a comprehensive list of measures). Each of these statistics is shown to the users as a 1D plot over time with a color code matching that of the segmentation in the 3D view. Then, if the users identify an irregular pattern in the curve of the time-varying statistics, they can directly inspect the corresponding finger in 3D (Fig. 5) and navigate through the corresponding time steps. We also provide *global* time-varying statistics computed over the set of fingers, or over the dissolving salt $\mathscr{S}$. As described in Sec. 5, for a given run, users typically first inspect the time-varying 1D plots and then further focus on the corresponding fingers/time steps with the time-varying 3D linked view. This addresses task 3 of the contest instructions [9].

3.5 Comparative analysis (across runs)

Our user interface also offers comparative analysis capabilities by supporting the side by side display of multiple time-varying *global* statistics (one per run), as well as 3D views that are linked to each of the time-varying statistics window (Fig. 6). Typically, users first inspect a summary view of the time-varying global statistics for *all* runs (Fig. 7). This enables the visual detection of repeating patterns across runs as well as outliers. Then, our interface enables the interactive inspection in comparative views of the time-varying fingers for the runs selected by the users. This addresses task 4 of the contest instructions [9].

4 Implementation

We implemented our data analysis framework in C++. In particular, processing tasks have been designed as VTK filters [11] which were globally handled by Python scripts. These scripts were run offline on commodity desktop computers to compute the finger extraction and tracking (Sec. 3.1 through Sec. 3.3) as well as the time-varying statistics (Sec. 3.4 and Sec. 3.5). We wrote ParaView plugins [10] to implement the user interface of our system.

The typical preprocessing time (Sec. 2) for a single run is approximately 2 hours, while the complete run time for our data analysis framework is approximately one hour per run. We applied our analysis pipeline to the 93 runs provided in the framework of the contest (22 high-res, 23 medium-res and 48 low-res runs). Regarding the exploration features of our framework, these run at interactive rates, as showcased in the companion video, which presents live captures that were shot in real time. This addresses task 5 of the contest instructions [9].

5 Results and Discussion

This section reports the findings we made by using our data analysis framework. In particular, we first focus our analysis on the 22 runs at high resolution (1.7M particles). The comparative analysis across resolutions (544k and 194k particles) is discussed in Sec. 5.3.

5.1 Regime identification

In this section, we first try to corroborate the decomposition of the fingering process in three regimes (Sec. 1). To do so, we will first inspect summary views of global statistics (Sec. 3.5) for all runs.

We first analyze the evolution of the descent of the dissolving salt, by looking at the minimum Z-coordinate of $\mathscr{S}$ through time (Fig. 7). Three major observations come out of this plot. First, the descent seems linear with time after time-step 10. Second, all runs behave identically in the early time-steps and only little differences can be observed towards the end of the process. Moreover, such a difference seems to increase linearly with time. Third, the 3 regimes identified in Sec. 1 (Launch, Expansion, Termination) are clearly visible: *Termination:* All runs hit the bottom of the domain in the same time-frame (time step 50 to 60), after which a mixing of the two fluids can be observed (see the companion video). *Launch:*

From time-step 0 to 10, the dissolving salt remains at the top of the domain; *Expansion:* From time-step 10 to 50-60, the dissolving salt travels down the domain.

To confirm the bounds of the launch regime, we inspect the evolution of the average salt concentration of the dissolving salt $\mathscr{S}$ (Fig. 8). These curve exhibit a clear inflection pattern in the early stages of the simulation, with a clear local maximum at time-step 10. We suspect this maximum marks the end of the launch phase. To confirm this hypothesis, we inspect in comparative mode (Sec. 3.5) the runs where the dissolving salt hits first (Run #19) and last (Run #15) the bottom of the domain. Fig. 9 shows in comparative views the extracted finger tips (green spheres) along with the geodesic distance to the top of the domain (f_d, blue to green color gradient). Note that the geometry of $\mathscr{S}$, the set of extracted finger tips and the level lines of f_d are highly similar in both runs in the early stage of the launch regime (time-step 5, top). This similarity quickly vanishes towards the end of the launch regime (time-step 10, bottom), where small amplitude fingers clearly start to appear (small bumps in $\mathscr{S}$, bottom). After this time-step, fingers clearly evolve independently in each run. Thus, we conclude that the launch regimes terminates at time-step 10 for all runs.

5.2 Characteristics of the expansion regime

In this section, we try to corroborate the description of the fingering process in the expansion regime (Sec. 1), where larger fingers are supposed to grow faster, at the expense of smaller ones, which they eventually absorb. To do so, we first inspect the evolution of the number of fingers through time (Fig. 10). This plot confirms that the number of fingers globally decreases for all runs, with a consistent decrease rate across runs, to eventually tend to a small number (typically five or less) towards the end of the expansion regime. Fig. 11 provides a comparative view for the fastest and slowest runs, which confirms the existence of only few, very large fingers at the end of the expansion regime. To further understand how fingers evolve during the expansion process, we inspect the evolution through time of the ratio between the volume of the largest finger and that of the dissolving salt $\mathscr{S}$ (Fig. 12). These curve indicate how the largest finger evolves in size for all runs. In particular, Runs #19 and #4 show a particularly large finger towards the end of the expansion process. We will focus on these to better understand the decrease in the number of fingers. Figs. 13 and 14 show comparative views before and after the merge of large fingers in Run #19 and #4 respectively. In particular, these figures show that the fingers that are further down the domain are also the fastest.

By further inspecting other finger merge events, we identified an unexpected behavior, that we call *detachment*, (Figs. 15 and 16 for Runs #19 and #4 respectively). In particular, these figures show that clearly prominent fingers, which are both the fastest and the deepest down the domain, can suddenly detach from the rest of the dissolving salt $\mathscr{S}$. This phenomenon is preceded by a sudden gain of velocity, which is accompanied by a dramatic drop down in salt concentration, eventually fully dissolving the finger in the ambient water. Our inspections reveal that such detachments occur several times in all runs, either early or late in the expansion. We suspect these may have an impact on the efficiency of the penetration of the less viscous fluid since the curves of average salt concentration indicate that detaching fingers instantly vanish and dissolve in the ambient water, suddenly stopping the progression of the dissolving salt in these regions (see Sec. 6 for further comments).

5.3 Inter-resolution analysis

In this section, we study the impact of the input data particle resolution on the characterization of the viscous fingering process. To do so, we visualize global summarizes provided by global time-varying statistics for all runs in Fig. 17. This figure plots, for the dissolving salt $\mathscr{S}$, the evolution over time of the minimimum Z-coordinate, the average salt concentration, the volume, the average velocity and the number of fingers. In particular, each of the three resolutions is represented with a distinct color. These three sets of curves exhibit similar global behaviors: a salt descent according to a linear slope (Fig. 17(a)), a linear decrease of salt concentration in the expansion regime (Fig. 17(b)) and a linear increase in both volume (Fig. 17(c)) and velocity (Fig. 17(d)). However, each resolution can be easily distinguished from the others as curves of the same color tend to cluster, with only few overlap with the other colors. This indicates clear distinctions between resolutions (see Sec. 6 for further comments).

6 Conclusion

In this paper, we have presented a topological data analysis framework, inspired by Laney et al. [12], that we adapted to the special case of the analysis of ensembles of particle data-sets representing viscous fingers. Our analysis pipeline is based on a volumetric interpolation of the particle data (Sec. 2), followed by a finger tip extraction based on persistent homology and a finger identification with the Morse complex (Sec. 3.2). The tracking through time of the fingers by overlap estimation (Sec. 3.3) enables the evaluation of relevant time-varying statistics (Secs. 3.4 and 3.5).

By using our data analysis framework on the data-sets provided in the context of the scientific visualization contest 2016 [9], we were able to corroborate the characterization of the viscous fingering process into three distinct regimes (launch, expansion, termination) for which we were able to specify the exact intervals of appearance. The interactive exploration features of our framework also enabled the quantitative validation of the characterization of the expansion regime, where the deepest fingers indeed grow the fastest, at the expense of the smaller ones that they eventually absorb. This explains the consistent decrease of the number of fingers through time. Additionally, we observed an unexpected behavior, that we called *detachment*, where fast, deep and with low salt concentration fingers suddenly detach from the rest of the dissolving salt. Our inter-resolution analysis revealed that simulation runs of distinct resolutions had globally similar behavior. However, later expansion starts, faster penetration rates and fewer viscous fingers were observed as the resolution decreases. This comparison shows that the similarity to the highest resolution runs (according to the above criteria) decreases with the resolution, suggesting a convergence of the simulation code for increasing resolutions.

In the future, we would like to validate our analysis framework with domain experts. Moreover, we would like to investigate the design of quantitative measures for a deeper evaluation of detachments, as we suspect they may have an impact on the efficiency of the penetration.

Acknowledgments

This work is partially supported by the Bpifrance grant "AVIDO" (Programme d'Investissements d'Avenir, reference P112017-2661376/DOS0021427) and by the French National Association for Research and Technology (ANRT), in the framework of the LIP6 - Kitware SAS CIFRE partnership reference 2015/1039.

References

[1] T. F. Banchoff. Critical points and curvature for embedded polyhedral surfaces. *The American Mathematical Monthly*, 1970.
[2] P. Bremer, G. Weber, J. Tierny, V. Pascucci, M. Day, and J. Bell. Interactive exploration and analysis of large scale simulations using topology-based data segmentation. *IEEE Transactions on Visualization and Computer Graphics*, 2011.
[3] T. Cormen, C. E. Leiserson, R. L. Rivest, and C. Stein. *Introduction to Algorithms*. MIT Press, 2009.
[4] L. De Floriani, U. Fugacci, F. Iuricich, and P. Magillo. Morse complexes for shape segmentation and homological analysis: discrete models and algorithms. *Computer Graphics Forum*, 2015.
[5] A. De Wit, Y. Bertho, and M. Martin. Viscous fingering of miscible slices. *Physics of Fluids*, 17(5), 2005. doi: 10.1063/1.1909188
[6] E. Dijkstra. A note on two problems in connexion with graphs. *Numerische Mathematik*, 1959.
[7] H. Edelsbrunner and J. Harer. *Computational Topology: An Introduction*. American Mathematical Society, 2009.
[8] J. Feder. *Viscous Fingering in Porous Media*, pp. 41–61. Springer US, Boston, MA, 1988. doi: 10.1007/978-1-4899-2124-6_4
[9] IEEEVIS. Scientific visualization contest. `http://www.uni-kl.de/sciviscontest/`, 2016.
[10] Kitware. Paraview. `http://www.paraview.org`, 2016.
[11] Kitware. The Visualization Tool Kit (vtk). `http://www.vtk.org`, 2016.
[12] D. E. Laney, P. Bremer, A. Mascarenhas, P. Miller, and V. Pascucci. Understanding the structure of the turbulent mixing layer in hydrodynamic instabilities. *IEEE Transactions on Visualization and Computer Graphics (Proc. of IEEE VIS)*, 2006.
[13] G. Reeb. Sur les points singuliers d'une forme de Pfaff complètement intégrable ou d'une fonction numérique. *Comptes-rendus de l'Académie des Sciences*, 222:847–849, 1946.
[14] D. Shepard. A two-dimensional interpolation function for irregularly-spaced data. In *ACM National Conference*, 1968.
[15] B. S. Sohn and C. L. Bajaj. Time varying contour topology. *IEEE Transactions on Visualization and Computer Graphics*, 2006.
[16] L. Vincent and P. Soille. Watersheds in digital spaces: an efficient algorithm based on immersion simulations. *IEEE Transactions on Pattern Analysis and Machine Intelligence*, 1991.

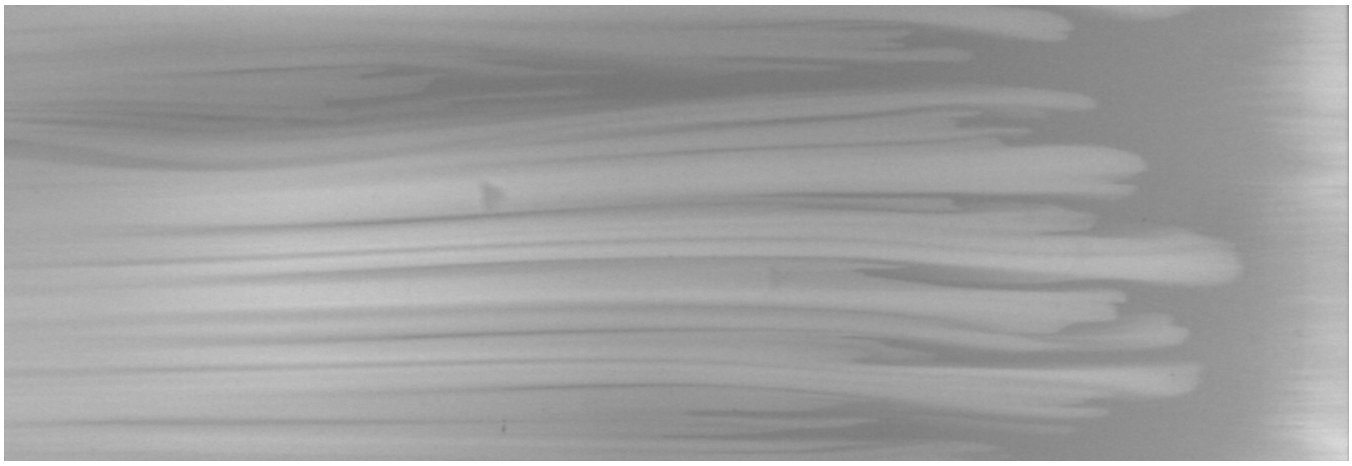

Figure 1: Photograph of viscous fingers in a glycerol-water mix (creative commons license).

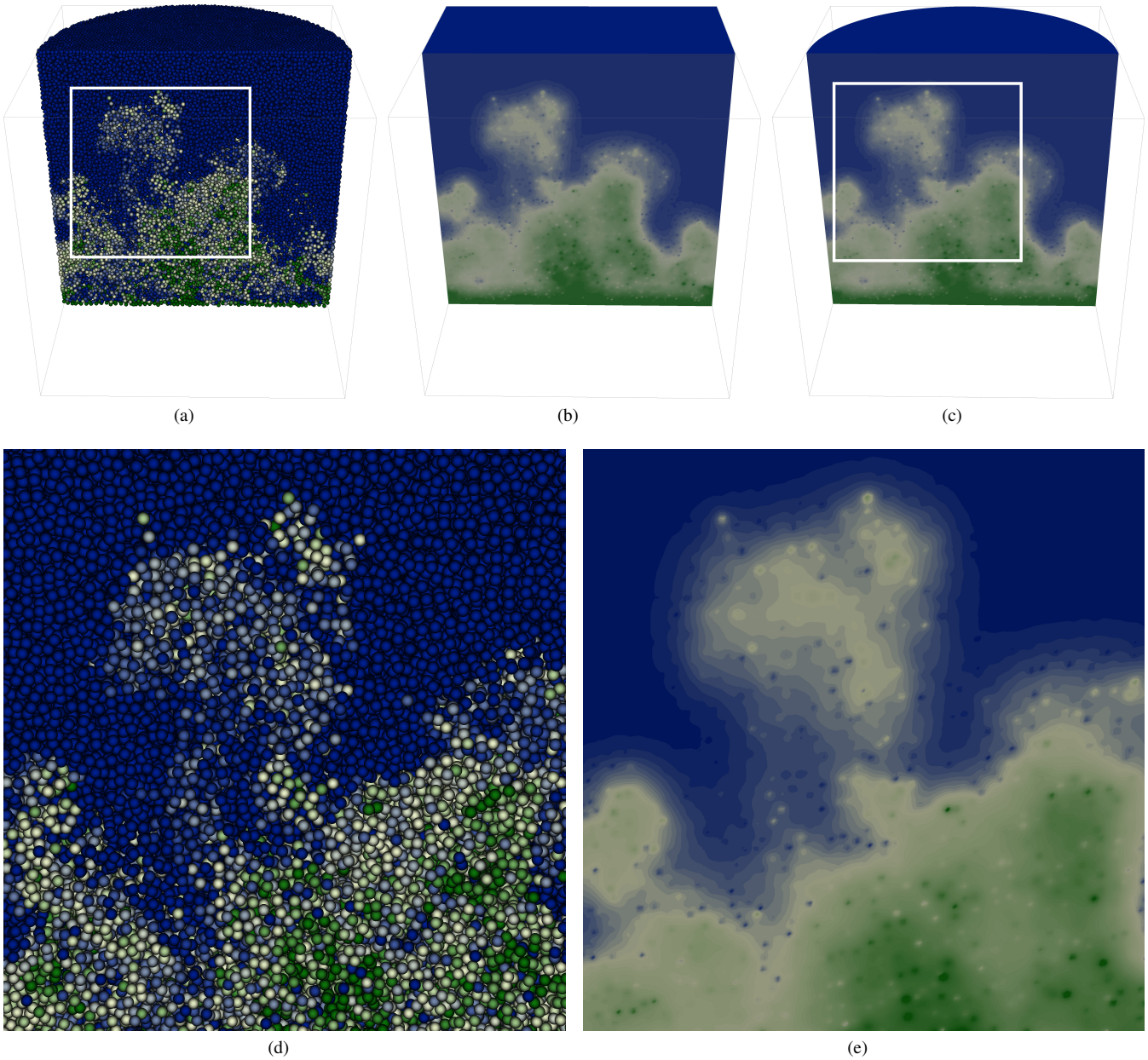

Figure 2: Preprocessing for each time-step. The input particle data is shown with small spheres (screen space rendering) and the salt concentration is shown with the color gradient (a). Particles are interpolated onto a regular grid with Shepard's method [14] (b). Next, the grid is clipped (c) to the original domain's shape (a cylinder) to avoid boundary effects. (d) and (e) show zoom-ins for the white square ((a and (b)). Data-sets are shown upside down to reduce occlusion.

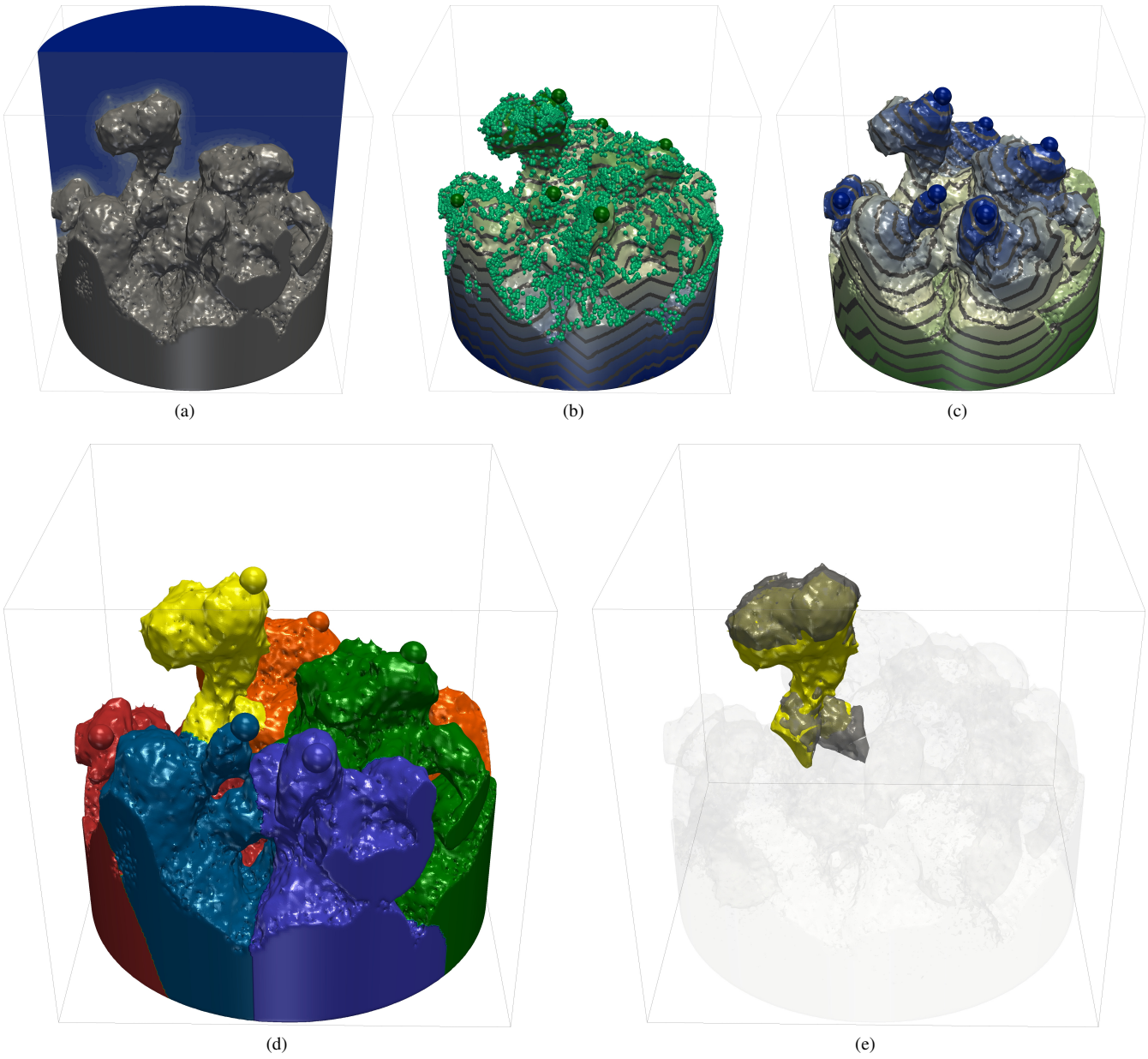

Figure 3: Overview of our topological data analysis pipeline. (a) The dissolving salt is first isolated from the ambient water by considering the largest connected component (noted $\mathscr{S}$, in gray) of the sur-level set of salt concentration (Sec. 3.1). (b) Finger tips are identified as local maxima (small light green spheres) of the geodesic distance $f_d : \mathscr{S} \to \mathbb{R}$ (color gradient and level lines) from the top of the cylinder. Restricting the identification to the most persistent maxima (larger dark green spheres) enables the identification of the most prominent fingers. (c) Geodesic distance field from the most persistent maxima $f_t : \mathscr{S} \to \mathbb{R}$. (d) The Morse complex of f_t decomposes $\mathscr{S}$ into fingers (Sec. 3.2). (e) Each finger at time step t is connected to the finger at time step $t+1$ which maximizes the volume of their intersection (Sec. 3.3). An example finger is shown in yellow while the corresponding maximizer at time step $t+1$ is shown in transparent black. Data-sets are shown upside down to reduce occlusion.

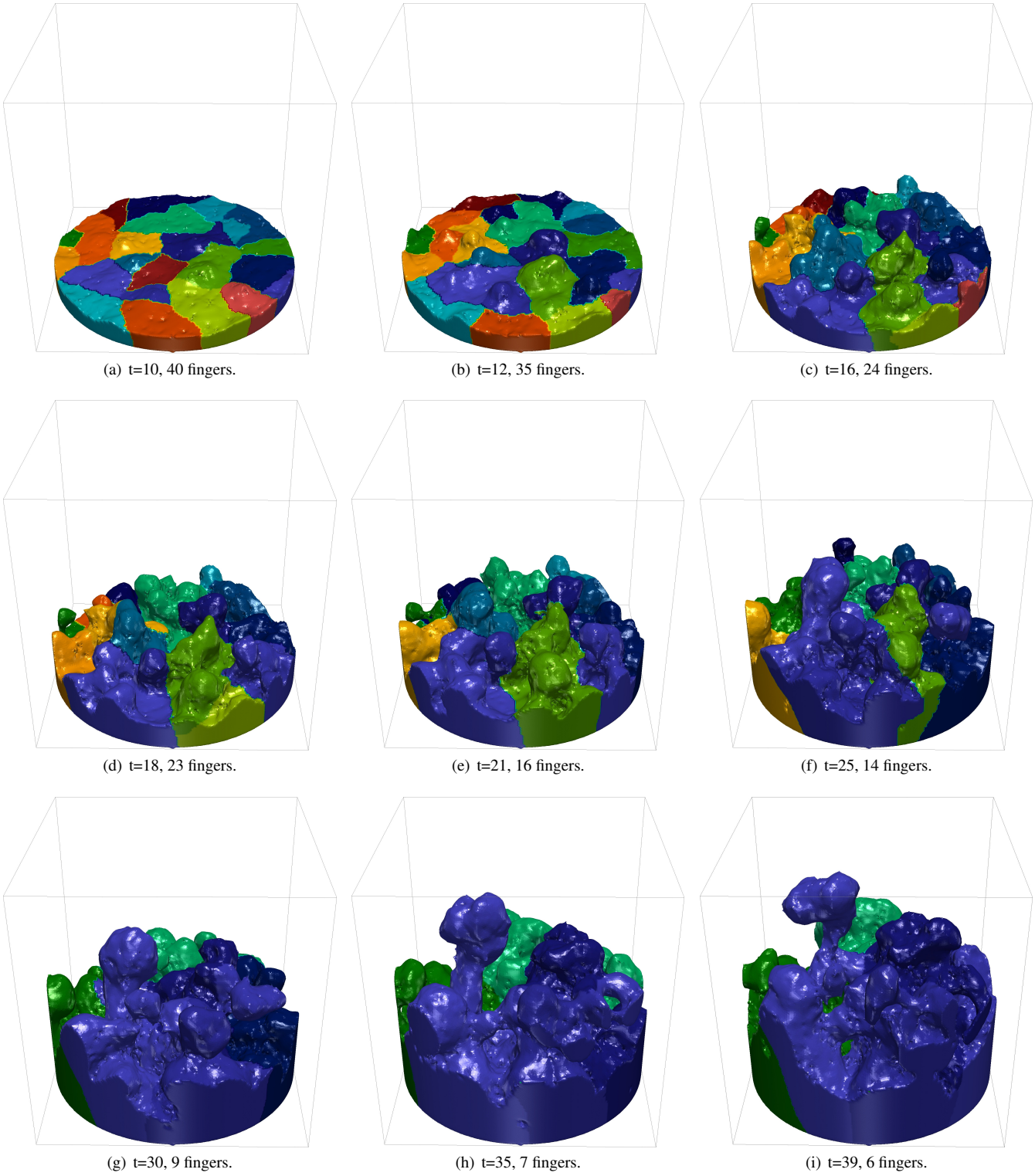

(a) t=10, 40 fingers. (b) t=12, 35 fingers. (c) t=16, 24 fingers.

(d) t=18, 23 fingers. (e) t=21, 16 fingers. (f) t=25, 14 fingers.

(g) t=30, 9 fingers. (h) t=35, 7 fingers. (i) t=39, 6 fingers.

Figure 4: Example of finger tracking through time on the run #3 of the lowest particle resolution. Fingers that are connected through time are shown with the same color.

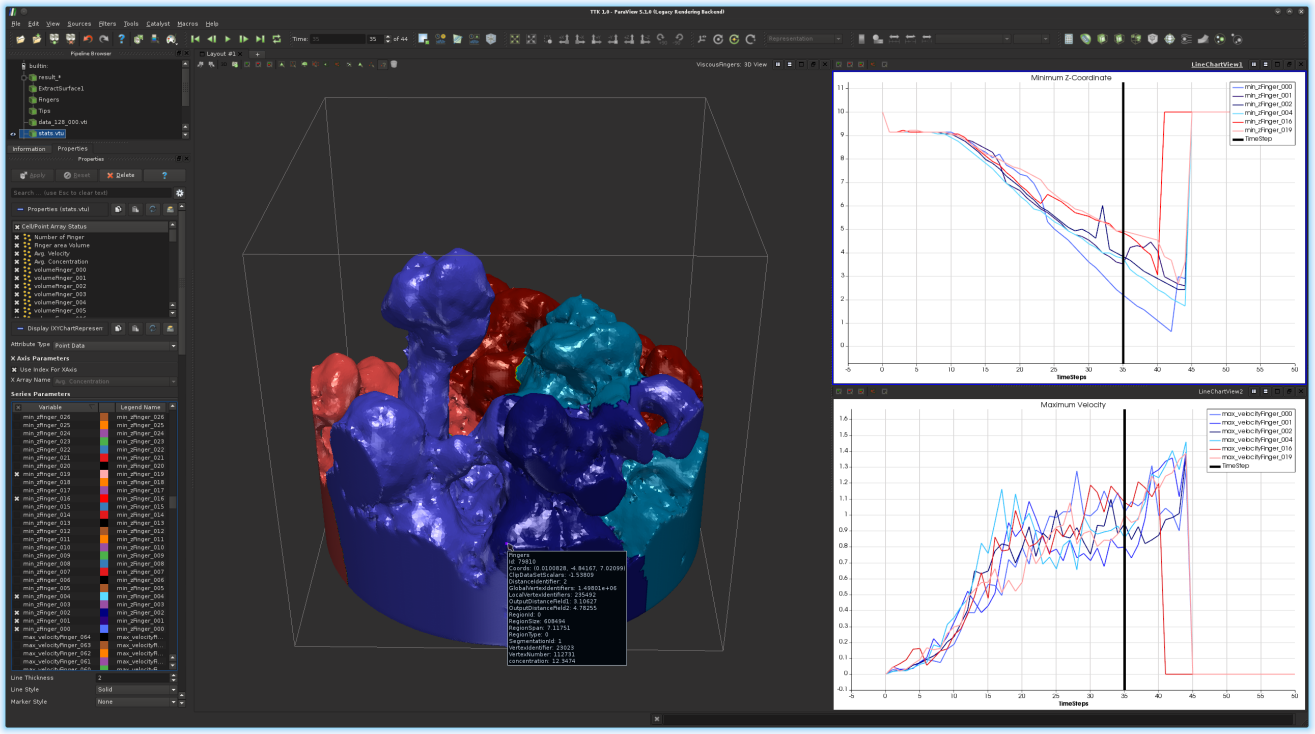

Figure 5: Screen-shot of the user interface to our data-analysis framework (intra-run mode). Users can select from the bottom-left list the *per-finger*, time-varying statistics to visualize on the right side of the screen (white background). There, the vertical black line indicates the time-step being currently visualized in the linked 3D view (center). Users can navigate through time steps with the time navigation buttons (top, center). Various per-finger statistics can be displayed in the 3D view by pointing on a finger with the cursor (dark rectangle).

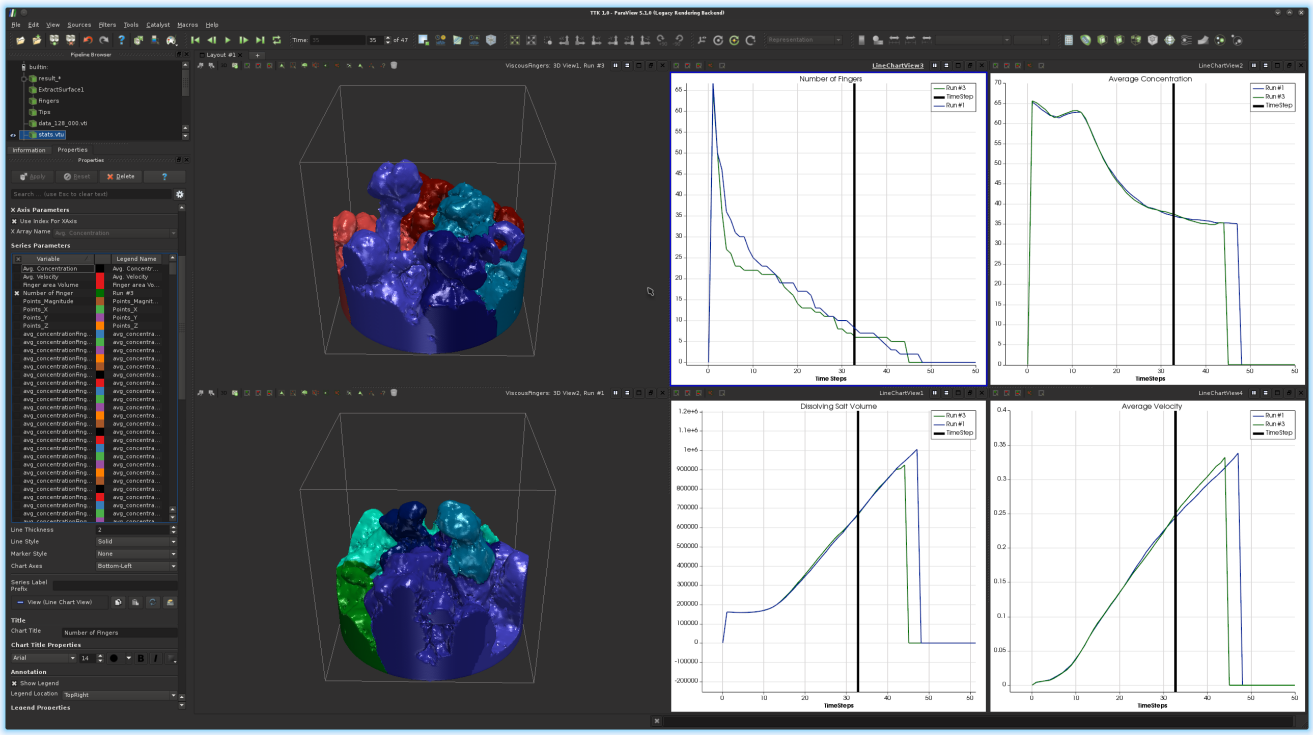

Figure 6: Screen-shot of the user interface to our data-analysis framework (comparative inter-run mode). Users can select from the bottom-left list the *global* time-varying statistics to visualize on the right side of the screen. In this case, the evolution of the number of fingers, of the fingers' volume, of average salt concentration and average velocity are shown for the runs #1 and #3 of the lowest particle resolution. There, the vertical black line indicates the time-step being currently visualized in the linked 3D views (center top: run #3, center bottom: run #1). Users can navigate through time steps with the time navigation buttons (top, center).

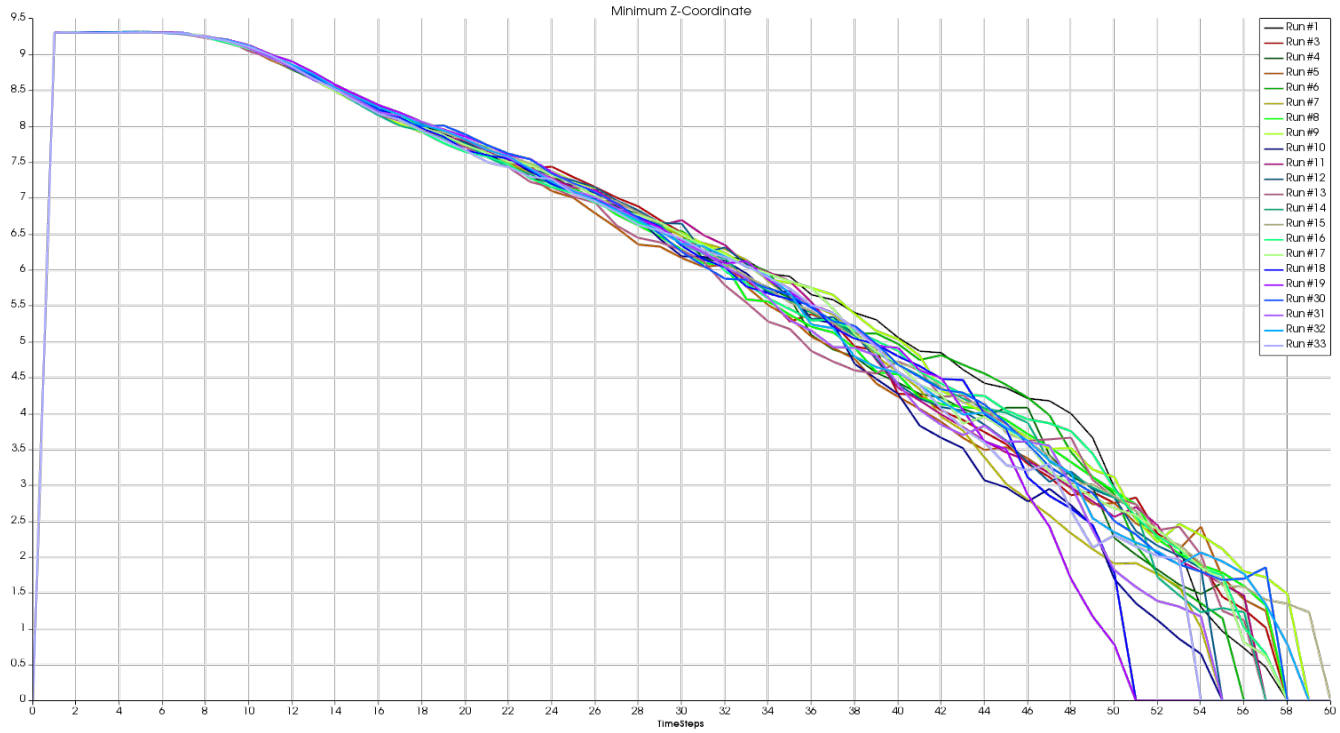

Figure 7: Evolution of the minimum Z-coordinate of the region of dissolving salt $\mathscr{S}$ for the 22 runs at high resolution. The descent evolution is linear through time (from time-step 10 to time-steps 50-60) and it is consistent across runs. For all runs, the dissolving salt is hitting the bottom of the domain in between time-steps 50 and 60.

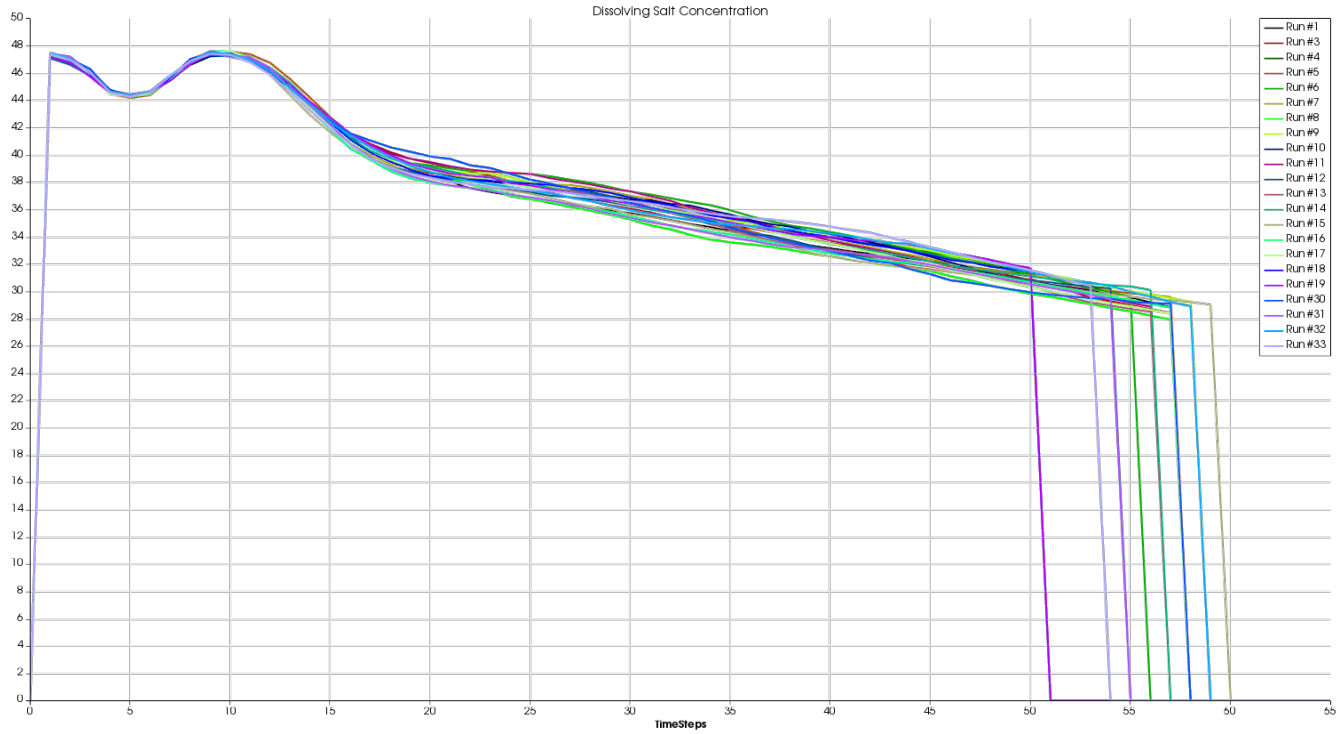

Figure 8: Evolution of the average salt concentration through time for the region of dissolving salt $\mathscr{S}$, for the 22 runs at high resolution. These curves exhibit a clear inflection pattern in the early stages of the simulation, with a clear local maximum of average concentration at time-step 10. This maximum seems to mark the end of the launch phase.

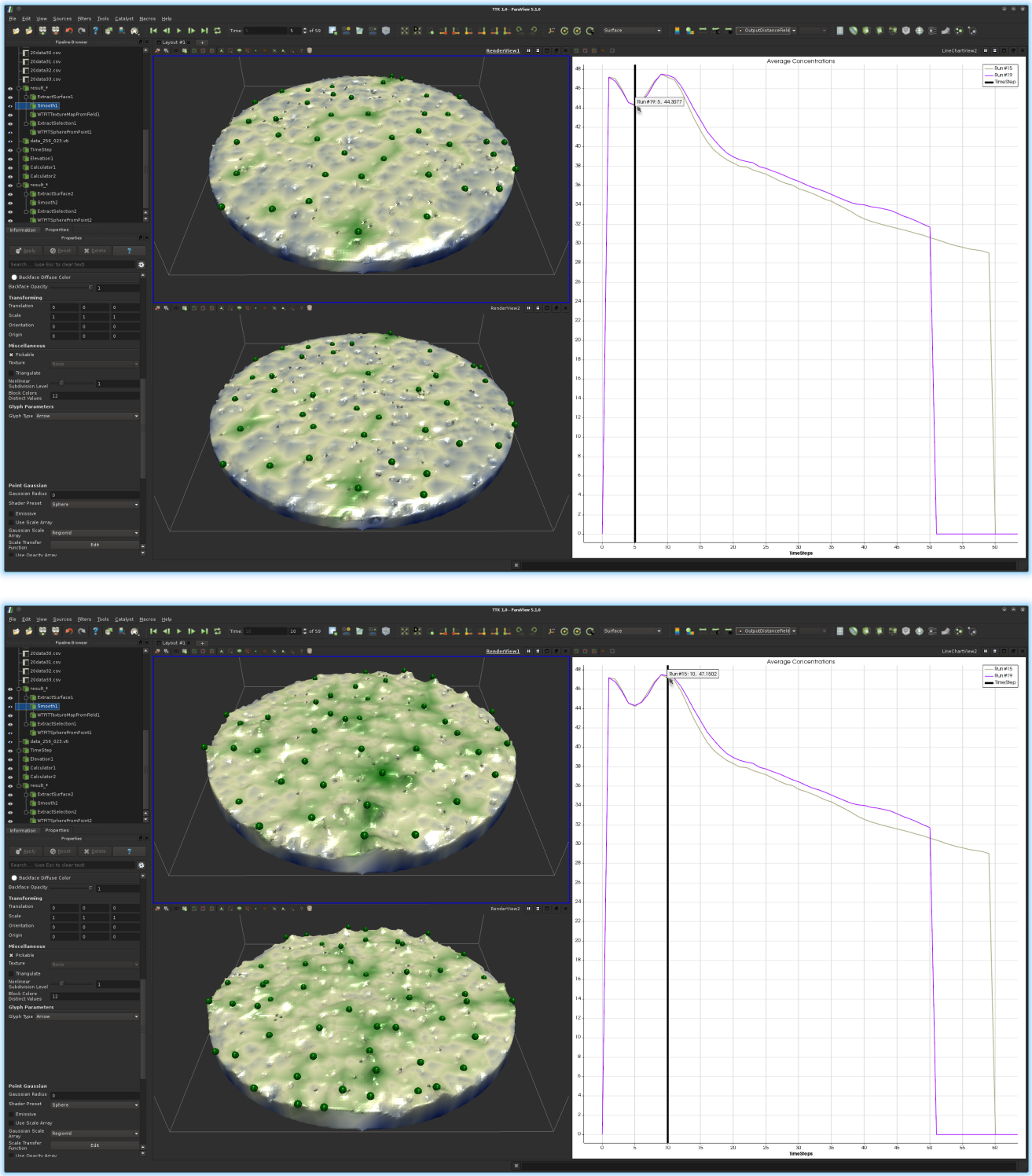

Figure 9: Interactive inspection of the launch regime in early and late time-steps (top: time-step 5, bottom: time-step 10) for the fastest and slowest runs (Run #19 and #15 respectively). The time-varying statistics window (right) plots the evolution of salt concentration in the region of dissolving salt $\mathscr{S}$. Despite the important difference in termination times (time-step 51 vs 60), both runs exhibit very similar patterns in the launch regime. The left 3D linked views show the corresponding regions $\mathscr{S}$, with the extracted finger tips (green spheres) and the geodesic distance to the top of the domain (f_d, blue to green color gradient). The geometry of $\mathscr{S}$, the set of extracted finger tips and the level lines of f_d look alike in both runs in the early stages of the launch regime (time-step 5, top). However, this similarity quickly vanishes towards the end of the launch regime (time-step 10, bottom), where small-amplitude fingers clearly start to appear (see the small bumps in $\mathscr{S}$ in the linked 3D views).

Figure 10: Evolution of the number of fingers through time for the 22 runs of the highest resolution. For all runs, this number globally decreases and converges towards a low number (typically five or less) towards the end of the expansion regime. Also note that the decrease rate is consistent across runs (similar slopes).

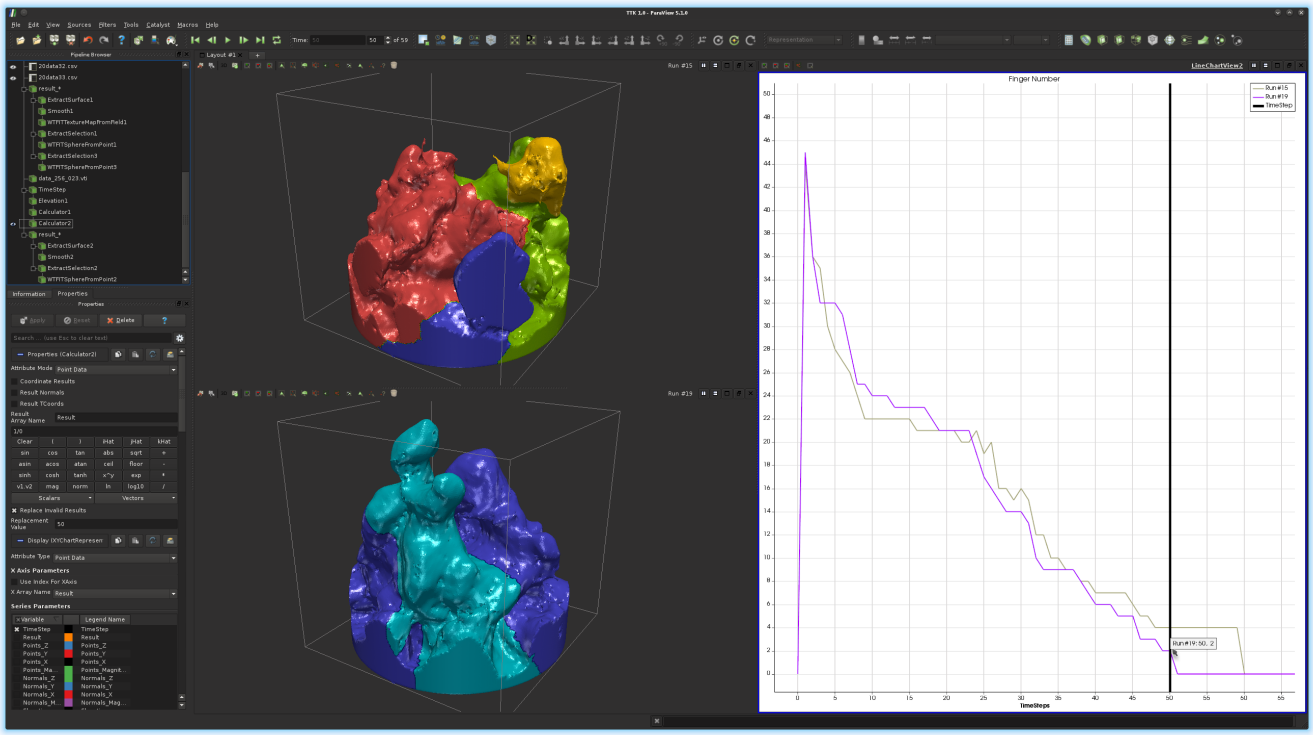

Figure 11: Extracted fingers at the end of the expansion regime for the fastest and slowest runs (Run #19 and #15 respectively) of the highest resolution. The 3D linked views indicate large prominent fingers (one color per finger) in both runs.

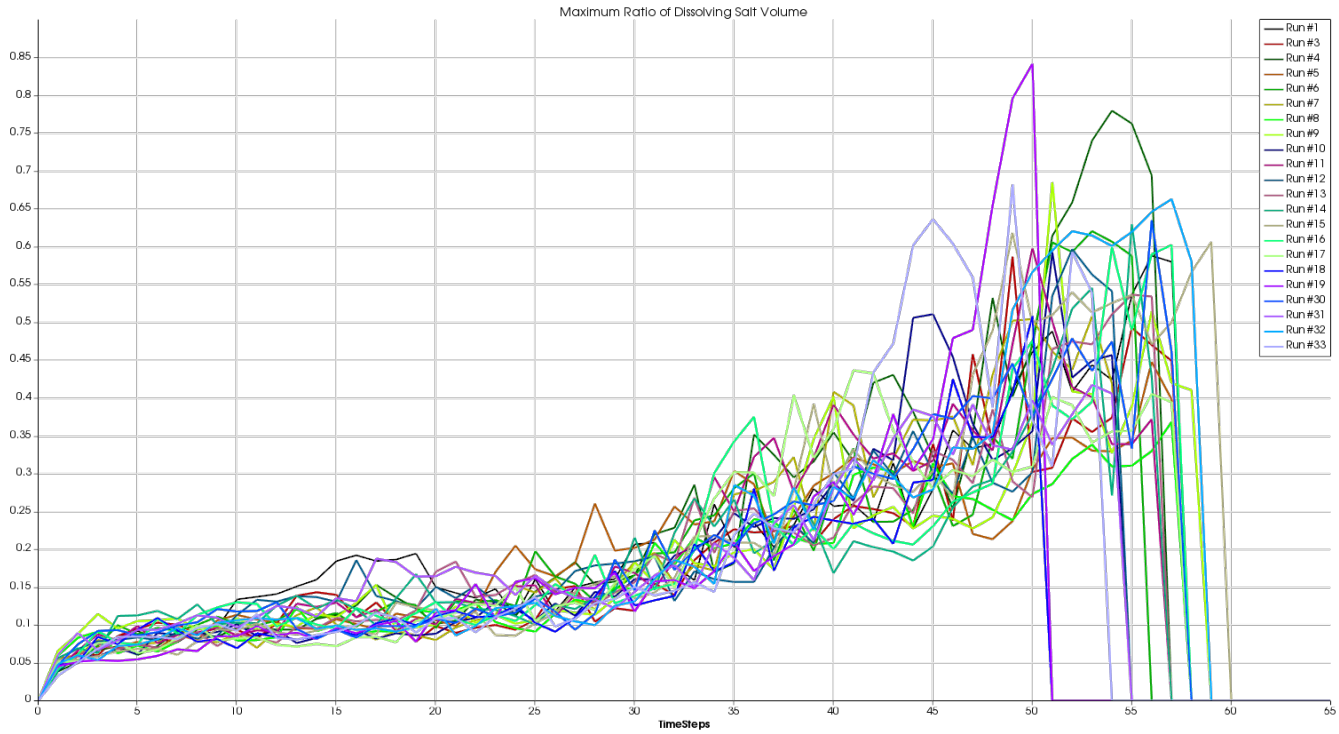

Figure 12: Evolution through time of the ratio between the volume of the largest finger and that of the dissolving salt $\mathscr{S}$, for the 22 runs of the highest resolution. These curve indicate how the largest finger evolves in size for all runs. In particular, Runs #19 and #4 show a particularly large finger towards the end of the expansion (time-steps 50, purple curve, and 54, dark green curve, respectively).

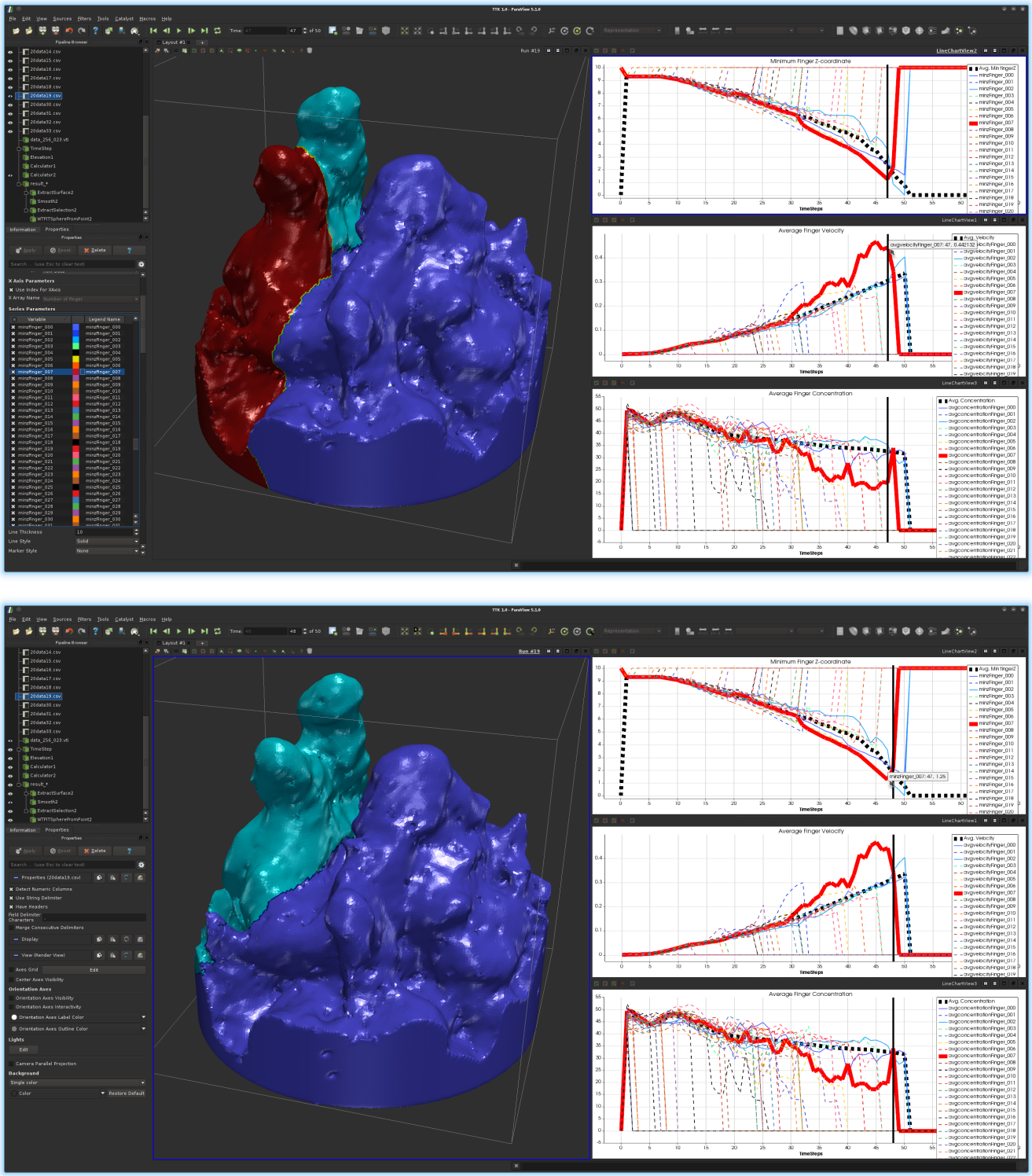

Figure 13: Merging of two large fingers in Run #19, before (top) and after (bottom). The 3D linked views show that the prominence of the red finger is not sufficient anymore for it to be identified as an independent finger after time-step 48. Technically, this is due to the fact that the persistence of the corresponding finger tip went below the admissible threshold. At this point, the cyan and red fingers are considered as merging. Time varying statistics are provided on the right side: minimum of Z-coordinate for each finger, average velocity for each finger and average salt concentration for each finger. These curves are shown with dash lines for fingers which are no longer active at the current time step. The bold black dash lines indicate global statistics for the region of dissolving salt $\mathscr{S}$. The bold, red curves indicate time-varying statistics for the red finger. In particular, these curve show that, before the merging, this finger was both the deepest down the domain (top curves) and the fastest (center curves).

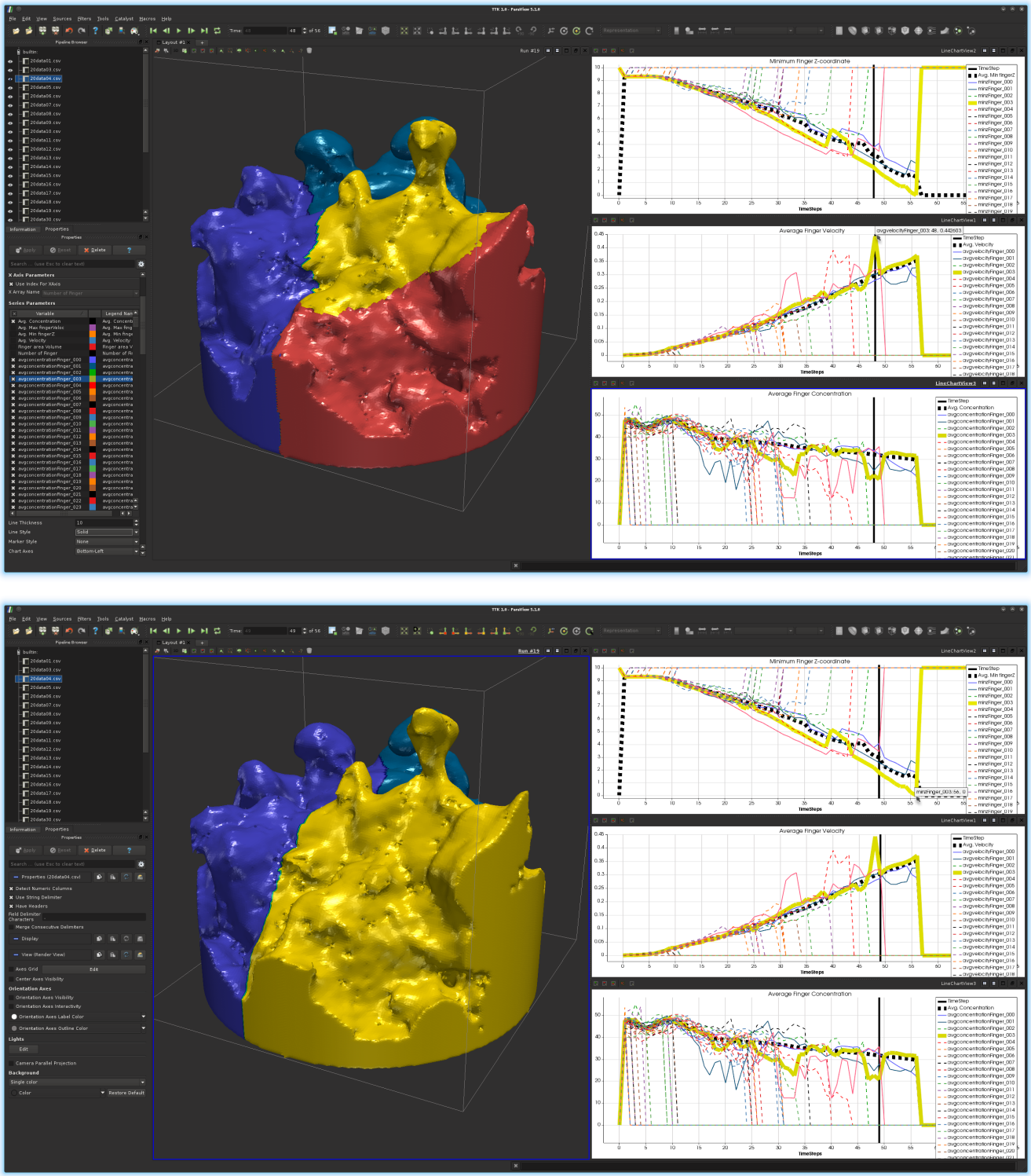

Figure 14: Merging of two large fingers in Run #4, before (top) and after (bottom). The 3D linked views show that the prominence of the red finger is not sufficient anymore for it to be identified as an independent finger after time-step 48. Technically, this is due to the fact that the persistence of the corresponding finger tip went below the admissible threshold. At this point, the yellow and red fingers are considered as merging. Time varying statistics are provided on the right side: minimum of Z-coordinate for each finger, average velocity for each finger and average salt concentration for each finger. These curves are shown with dash lines for fingers which are no longer active at the current time step. The bold black dash lines indicate global statistics for the region of dissolving salt $\mathscr{S}$. The bold, yellow curves indicate time-varying statistics for the yellow finger. In particular, these curve show that, before the merging, this finger was both the deepest down the domain (top curves) and the fastest (center curves).

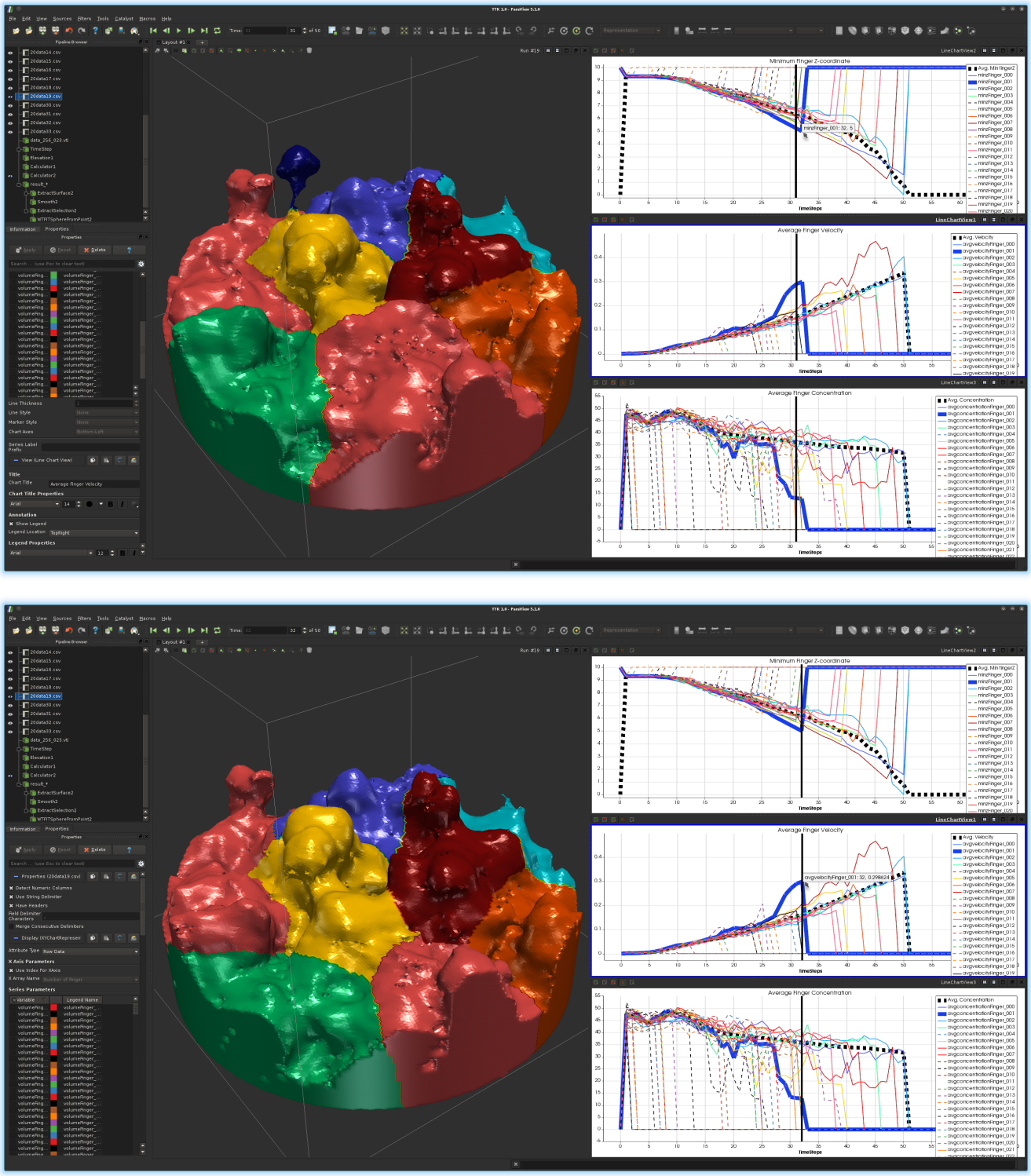

Figure 15: Finger detachment (dark blue finger) at time-step 32 of Run #19 (top: before, bottom: after). The 3D linked views show a clear prominence of the dark blue finger, despite a the very thin portion that connects it to the rest of the dissolving salt $\mathscr{S}$. This portion becomes so thin at time-step 32 that this finger gets disconnected from $\mathscr{S}$ and is therefore no longer considered as a finger by our analysis pipeline. We call such a phenomenon *detachment*, since a rapid finger grows so fast that it detaches from the rest of dissolving salt $\mathscr{S}$ and rapidly vanishes in the ambient water. Time varying statistics are provided on the right side: minimum of Z-coordinate for each finger, average velocity for each finger and average salt concentration for each finger. These curves are shown with dash lines for fingers which are no longer active at the current time step. The bold black dash lines indicate global statistics for the region of dissolving salt $\mathscr{S}$. The bold, dark blue curves indicate time-varying statistics for the dark blue finger. In particular, these curve show that, before detachment, this finger was both the deepest down the domain (top curves) and the fastest (center curves). Moreover, the bottom curves show that this finger had a dramatic drop down of salt concentration (bottom curves) exactly when it started to accumulate speed (time-step 27), to eventually fully dissolve in the ambient water.

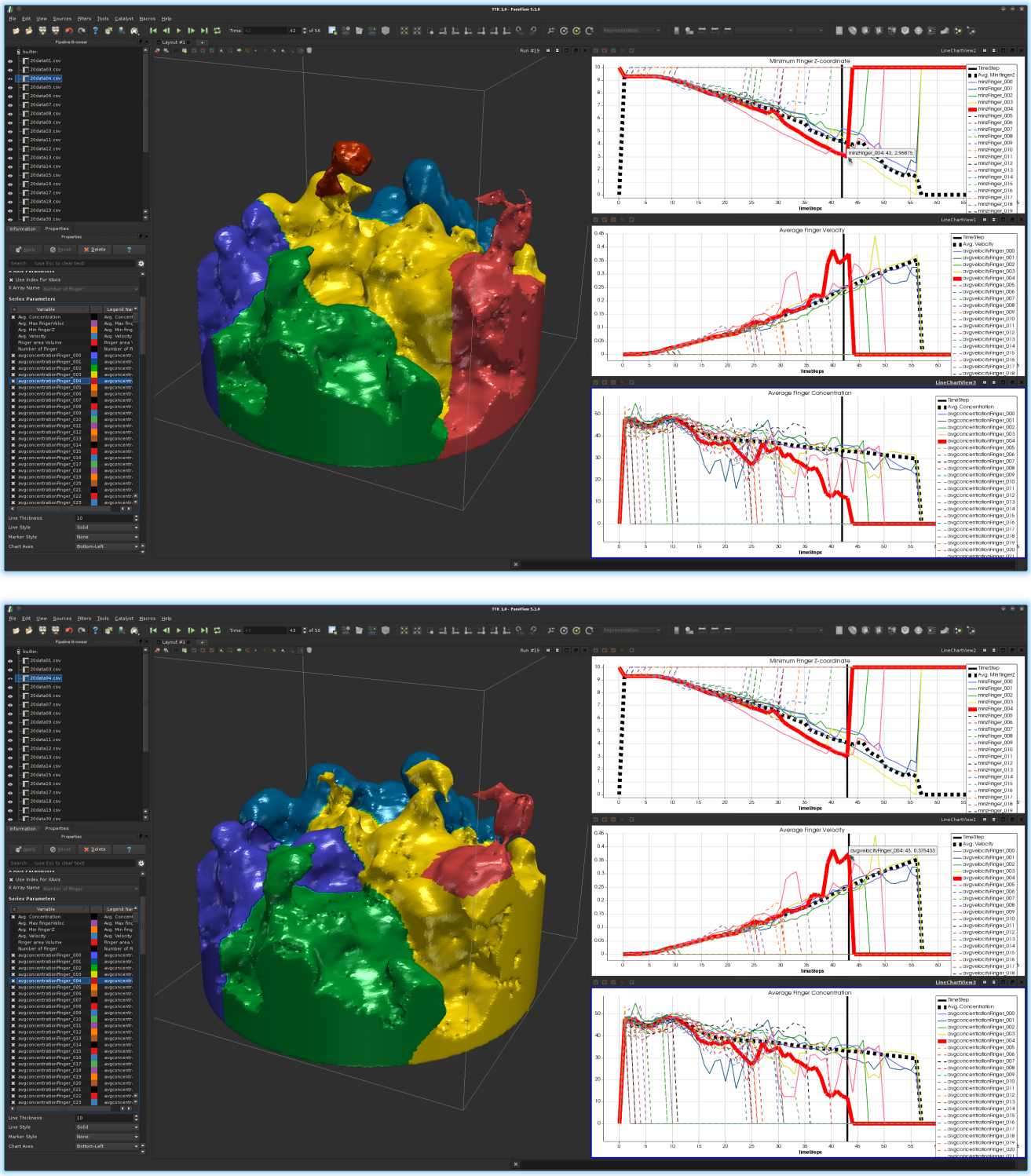

Figure 16: Finger detachment (dark red finger) at time-step 43 of Run #4 (top: before, bottom: after). The 3D linked views show a clear prominence of the dark red finger, despite a the very thin portion that connects it to the rest of the dissolving salt $\mathscr{S}$. This portion becomes so thin at time-step 43 that this finger gets disconnected from $\mathscr{S}$ and is therefore no longer considered as a finger by our analysis pipeline. We call such a phenomenon *detachment*, since a rapid finger grows so fast that it detaches from the rest of dissolving salt $\mathscr{S}$ and rapidly vanishes in the ambient water. Time varying statistics are provided on the right side: minimum of Z-coordinate for each finger, average velocity for each finger and average salt concentration for each finger. These curves are shown with dash lines for fingers which are no longer active at the current time step. The bold black dash lines indicate global statistics for the region of dissolving salt $\mathscr{S}$. The bold, dark red curves indicate time-varying statistics for the dark red finger. In particular, these curve show that, before detachment, this finger was both the deepest down the domain (top curves) and the fastest (center curves). Moreover, the bottom curves show that this finger had a dramatic drop down of salt concentration (bottom curves) exactly when it started to accumulate speed (time-step 38), to eventually fully dissolve in the ambient water.

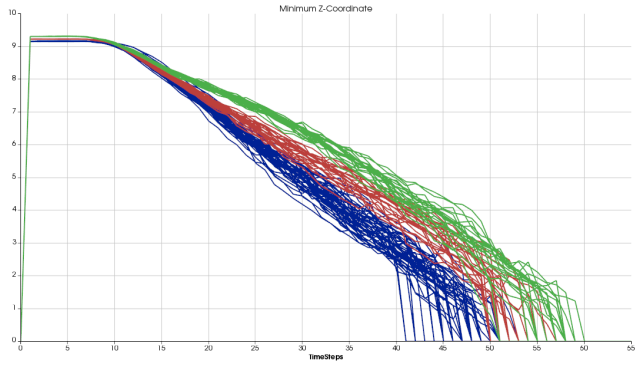

(a)

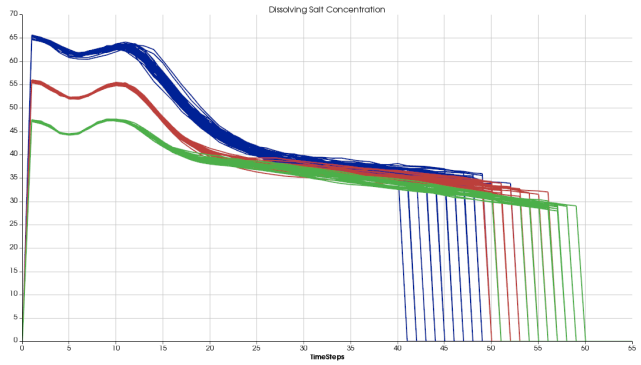

(b)

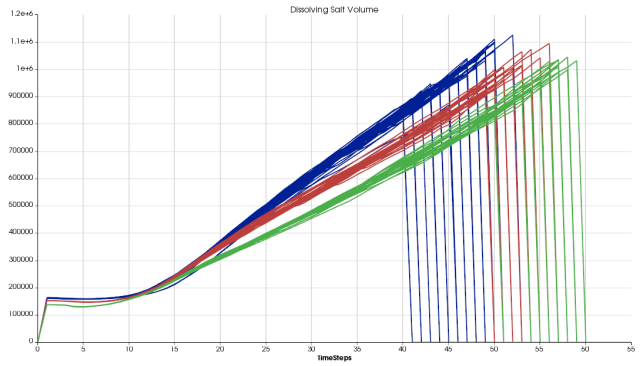

(c)

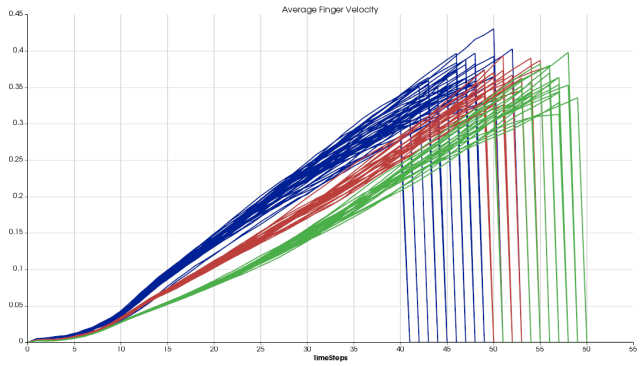

(d)

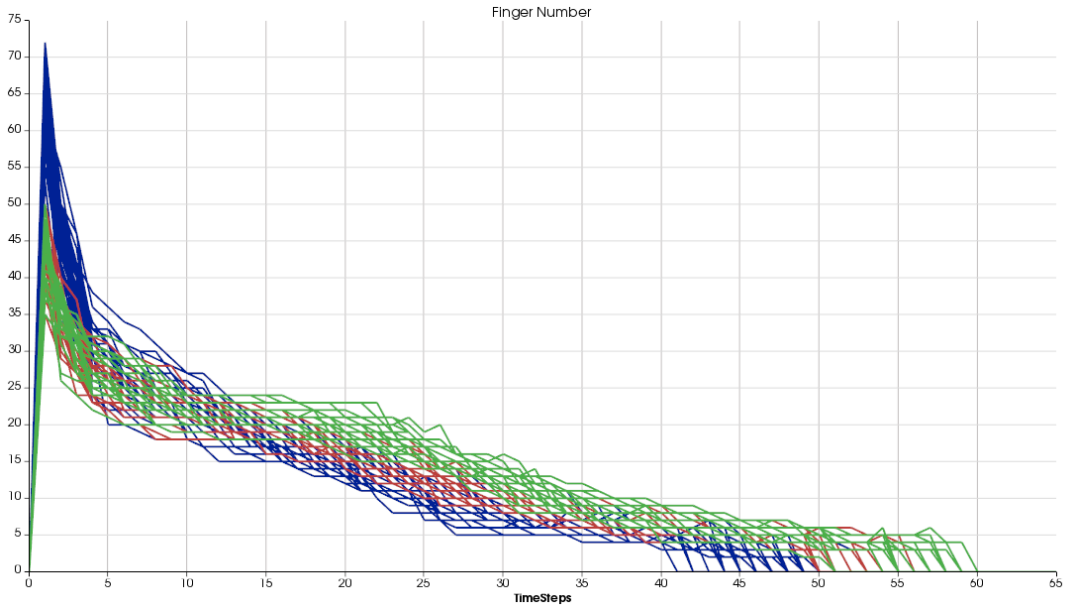

(e)

Figure 17: Global statistics as a function of time for the 22 high-res (green curves), 23 medium-res (red curves) and 48 low-res (blue curves) runs. These three sets of curves exhibit similar global behaviors: a salt descent according to a linear slope (Fig. 17(a)), a linear decrease of salt concentration in the expansion regime (Fig. 17(b)) and a linear increase in both volume (Fig. 17(c)) and velocity (Fig. 17(d)). However, each resolution can be easily distinguished from the others as curves of the same color tend to cluster, with only few overlap with the other colors. This indicates clear distinctions between resolutions. (a) The minimum Z-coordinate of the dissolving salt $\mathscr{S}$ indicates clearly distinct descent rate for the deepest fingers (different slopes). Here lower resolutions hit the bottom of the domain faster. (b) The average salt concentration of the dissolving salt $\mathscr{S}$ indicates clearly distinct initial salt concentration levels, with a slight delay for the start of the expansion regime (local maximum of concentration) as the resolution decreases. Note that from the middle of the expansion regime onward, the decrease rate is similar across resolutions. (c) The volume of the dissolving salt $\mathscr{S}$ also indicates different growth rate (lower resolutions grow faster, as suggested by (a)). (d) The average velocity within the dissolving salt $\mathscr{S}$ also indicates different average speeds, confirming the increase in speed for lower resolutions. (e) The evolution of the number of fingers indicates a clear distinction for the lowest resolution in the early time-steps. However, this increase is not confirmed in the expansion regime (typically around time-step 25), where fewer fingers are extracted as the resolution decreases. In conclusion, runs of distinct resolutions exhibit similar global behavior, however with later expansion starts, faster penetration rates and fewer viscous fingers as the resolution decreases. This comparative study shows that the similarity to the highest resolution runs (according to the above criteria) decreases with the resolution, suggesting a convergence of the simulation code for increasing resolutions.